CrossMark

Fabrication of functionalized graphene oxide/maleic anhydride grafted polypropylene composite film with excellent gas barrier and anticorrosion properties

Xuyang Li[a], Parthasarathi Bandyopadhyay[a], Thanh Tuan Nguyen[a], Ok-kyung Park[a],*, Joong Hee Lee[a,b],**

[a] Advanced Materials Institute of BIN Convergence Technology (BK21 Plus Global) & Dept. of BIN Convergence Technology, Chonbuk National University, Jeonju, Jeonbuk, 54896, Republic of Korea
[b] Carbon Composite Research Centre, Department of Polymer - Nano Science and Technology, Chonbuk National University, Jeonju, Jeonbuk, 54896, Republic of Korea

ARTICLE INFO

ABSTRACT

The octadecylamine (ODA) modified graphene oxide (mGO-ODA)/maleic anhydride grafted polypropylene (MAPP) composites (mGO-ODA/MAPP) were prepared and applied successfully as gas barrier and corrosion protection coating materials for the first time. The hydrophobic mGO-ODA sheets showed improved solubility in non-polar solvents with molar absorptivity was found to be 36 mL mg^{-1} cm^{-1} in ethylcyclohexane. FTIR analysis confirmed that mGO-ODA chemically interacts with MAPP. The mGO-ODA nanosheets were well exfoliated and dispersed in the MAPP matrix as confirmed by XRD analysis. The mGO-ODA/MAPP composites were coated on modified nylon sheets by a spray coating method, and the gas transmission rates (GTRs) of H_2 and O_2 were tested for these coated films. Cross-sectional FESEM showed the excellent attachment of these composite with the nylon film. The 60% mGO-ODA/MAPP-coated nylon film exhibited 93% and 112% improvement in elastic modulus values than the MAPP-coated and pure nylon films, respectively. Besides, 60% mGO-ODA/MAPP exhibited 94.1% and 95.0% reduction for H_2GTR and O_2GTR, respectively, compared to the pure nylon film. In addition, mGO-ODA/MAPP coated steel substrate exhibited excellent anticorrosion performance. The corrosion inhibition efficiency and corrosion rate were calculated to be 99.15% and 2.26×10^{-3} mm/year, respectively, for 60% mGO-ODA/MAPP.

1. Introduction

One of the greatest challenges of the 21st century is the development of alternative energy sources, and the scientific community has focused on using alternative renewable energy sources, like hydrogen gas (H_2), to substitute fossil energy resources. But, the safe storage and transport of H_2 is a very challenging task, due to its highly flammable nature and small molecular size with very high solid-state mobility in both metallic and polymeric material [1–5]. Improvement of the oxygen (O_2) and moisture barrier in polymer packaging materials is crucial for their application in food packaging, pharmaceutical, and flexible electronics [6–10]. Polymers have become the barrier materials of choice owing to their light weight, flexibility, low-priced, and easy processability compared to glass, metalized films, and SiO_x coatings. However, fabrication of high H_2 and O_2 barrier polymer thin films are extremely challenging because of the poor gas barrier properties of most of the polymers. Polymer composites reinforced by graphene-based materials have gained remarkable research interests due to the ultrahigh aspect ratio, gas impermeability and unique combination of thermal, electrical and mechanical properties of two-dimensional graphene [11–13]. Graphene makes an impermeable barrier to different gas molecules and it can act as a normal diffusion barrier between metal and corrosive materials during corrosion [13,14]. Bolotin et al. reported that graphene coating on the metal surface could efficiently inhibit oxidation of metal and they reported that anticorrosion efficiency of graphene coated copper films highly improved in an aerated Na_2SO_4 solution than bare copper [15]. Besides, they stated that multilayer-coated and four layers-coated graphene films on nickel surfaces corrode twenty and four times slower, respectively, than bare nickel. Shin et al. reported that oxidation resistance of reduced graphene oxide (rGO)-

coated metal (Fe and Cu foils) was improved than bare metal due to the inhibition of diffusion of H_2O, O_2, and other oxidants through rGO [16]. Birbilis et al. examined barrier performance of graphene-coated nickel and copper samples in an aqueous solution by electrochemical methods. They found anticorrosion performance of these coated films improved significantly compared to the bare metals [17]. Graphene produced by chemical vapor deposition (CVD-graphene) can be used as the excellent anticorrosion coating material, but it cannot be used as a long-term anticorrosion coating material because CVD-graphene can stimulate metal corrosion due to the coating defects [13,18]. In this context, incorporating graphene into polymer matrix to fabricate graphene/polymer composite is a promising method to combine the properties of graphene for anticorrosion [13,14]. It is expected that incorporation of highly hydrophobic graphene in hydrophobic polymer matrix could provide excellent barrier and anticorrosion performances. The hydrophobic graphene/polymer composites can show not only improved barrier properties which are helpful to inhibit the corrosion but also produced higher mechanical properties and thermal stabilities [2,6,14,19–23]. The barrier property of graphene/polymeric composites is improved due to the "tortuous path effect" for diffusing penetrants [2,7]. The tortuosity of diffusion path for penetrants depends on the amount, aspect ratio, and morphologies of the filler, as well as the interfacial interaction between filler and polymer matrix. The uniform dispersion of graphene (large aspect ratio) as well as excellent interaction with the polymer matrix can produce high barrier graphene/polymeric composites. The chemically modified graphene improves their interfacial interaction with the polymer matrix to the point of complete dispersion and successfully reinforces the polymer matrix, resulting in improved functional properties [6,24,25]. The octadecylamine (ODA) can simultaneously reduce and functionalize graphene oxide (GO) to highly hydrophobic modified graphene oxide (mGO-ODA), without the use of toxic reducing agents [26]. Polypropylene (PP) is a very important polyolefin, and has been widely used in many fields [27–29]. The interfacial interaction between graphene and hydrophobic polyolefin can be enhanced through surface modification of graphene nanosheets, or functionalization of polyolefin chains. In this study, maleic anhydride grafted polypropylene (MAPP) was used as polymer matrix because it's high hydrophobicity and polar maleic anhydride moiety. The covalent grafting of ODA moiety helps to bound mGO-ODA strongly with the MAPP and also enables complete dispersion of mGO-ODA in MAPP, resulting in improved gas barrier and anticorrosion properties. However, the fabrication of graphene based polymer composite coatings is still confronted due to corrosion-promotion property of graphene [13]. In this context, ODA and MAPP can completely cover up the graphene sheets, minimizing the direct contact between graphene and metal. Besides, ODA (act as a spacer) inhibits the connections between the graphene sheets, and these connections can enhance the conductivity of the composite. It is expected ODA and MAPP can able to minimize the corrosion-promotion activity of graphene.

Nylon films are ideally suited for applications in different fields, such as textile fibers, tape, retort packaging, food packaging, balloons and electronics, pharmaceutical and automotive parts [2,25,30]. However, high permeability values for reactive gases and moisture through the nylon film limit its application. Therefore, it is expected that deposition of hydrophobic graphene-based material may enhance the hydrophobicity of nylon surface materials, resulting higher barrier properties towards moisture and different gases through nylon film. There are many reports in the literature regarding polyethylene terephthalate (PET) film as substrate material to prepare graphene/polymer-coated PET film for gas barrier study, but studies of gas barrier using nylon as substrate can scarcely be found in the literature [1,3,4,8,31,32]. It is well-known that PET films have been utilized for the coating of hydrophilic materials from their aqueous solution. However, research based on the coating of nylon film with graphene-based hydrophobic material deserve to be developed because the nylon

film is microwaveable, recyclable, and burns without releasing harmful chemicals into the atmosphere.

Based on the above knowledge, it is expected that composite (mGO-ODA/MAPP) of mGO-ODA and MAPP could be suitable to prepare super gas barrier and anticorrosion coating materials. A series of mGO-ODA/MAPP composites were prepared using different amounts of mGO-ODA with a fixed amount of MAPP. The composites were coated on nylon film by spray-coating, to measure the hydrogen and oxygen gas transmission rates (GTRs) of these coated films. A facile spray coating technique was also used to prepare mGO-ODA/MAPP-coated film onto the stainless steel (SS) surface. MAPP (adhesion promoter) improves the attachment of the composite film with the nylon sheet and the steel surface. The dispersed mGO-ODA sheets in the MAPP matrix could increase the tortuosity of the diffusion pathway of penetrants (gas molecule and corrosive materials); thereby, it is expected that the present approach can considerably improve the anticorrosion performance and gas barrier property of the composite. The thermal stability, mechanical, and gas barrier properties, as well as anticorrosion performance of the nanocomposites, were investigated to study the potential of these nanocomposites in practical applications, including polymer packaging and protection of metals. Besides, an attempt has also been taken to correlate the anticorrosion performance and gas barrier property based on the gas barrier-improved mechanism.

2. Experimental

2.1. Materials

Maleic anhydride grafted polypropylene (MAPP, HGW95/3JB) was purchased from Lotte Chemical Co. Korea. Graphite was purchased from Sigma Aldrich, Germany. Kolon Kopa@ KN173HI Nylon 6 Resin film was used as a substrate for spray coating with composites. Octadecylamine (ODA), ethanol, acetone, hydrogen peroxide (H_2O_2), ethylcyclohexane (EC), hydrochloric acid (HCl), sulfuric acid (H_2SO_4), potassium permanganate ($KMnO_4$), and trichloroacetic acid were purchased from Samchun Pure Chemical Co. Ltd., South Korea. All the above reagents were analytical grade, and were used without further purification. Modification of the nylon surface is provided in the Supplementary Information. The steel samples (1.5 cm × 3 cm) were ground with 300–1200 μm emery papers and polished with an Al_2O_3 solution. The samples were finally ultrasonically cleaned using distilled water (DI water), acetone, and ethanol for 10 min, respectively.

2.2. Preparation of mGO-ODA

Graphite oxide was prepared from natural graphite flakes using modified Hummers method (Supplementary Information) [33,34]. The graphite oxide (200 mg) was taken in 250 mL beaker and mixed with DI water (200 mL), followed by ultrasonic treatment for 1 h to form stable brown GO suspension. The brown GO suspension was transferred to a 500 mL three-neck round-bottom flask equipped with reflux condenser and a stirring bar. Then, 600 mg of ODA was dissolved in 20 mL of ethanol. The ODA solution was slowly added to the GO suspension, followed by ultrasonic treatment for 1 h at room temperature. The resulting mixture was then refluxed with mechanical stirring for 15 h at 90 °C. The resulting black precipitate was filtered using a 0.2-μm PTFE membrane and washed several times with ethanol and DI water. The black product (mGO-ODA) was collected by drying at 60 °C in a vacuum oven for three days.

2.3. Preparation of mGO-ODA/MAPP composite-coated nylon films

At first, a measured amount of mGO-ODA (filler) was dispersed in ethylcyclohexane (EC) by ultrasonication in water (ice-cold) bath for 1 h to prepare uniform dispersion of filler in EC. Then, the 1 mL quantity of the mGO-ODA solution was dried at 60 °C in vacuum oven

and measured the weight of the dried mGO-ODA filler. The concentration of the mGO-ODA solution was found to be 5 mg/mL. A fixed amount (50 mg) of MAPP was added in 3 mL of EC and stirred to dissolve at room temperature. The different mGO-ODA/MAPP composite solutions were prepared by mixing different amounts of mGO-ODA solution (1.5, 3, 4.5 and 6 mL) into a fixed amount of MAPP (50 mg in 3 mL of EC) solution. Next, the composite solutions were sonicated for 2 h to obtain the homogeneous solutions. The modified nylon sheets were coated by spraying the composite solutions at 50 °C using a spray gun under constant pressure. Afterward, the coated films were dried under a flow of air. During the spray coating, the distance between the spray gun and nylon film remained fixed. The composites contained 15, 30, 45, and 60 wt% of mGO-ODA (with respect to MAPP) are denoted 15% mGO-ODA/MAPP, 30% mGO-ODA/MAPP, 45% mGO-ODA/MAPP, and 60% mGO-ODA/MAPP, respectively. The amounts of mGO-ODA in 15% mGO-ODA/MAPP, 30% mGO-ODA/MAPP, 45% mGO-ODA/MAPP, and 60% mGO-ODA/MAPP were 7.5, 15, 22.5, and 30 mg, respectively. The pure MAPP (50 mg) and mGO-ODA (30 wt%)-coated nylon films were also prepared using the similar method as mentioned above, by spraying pure MAPP and mGO-ODA solutions, respectively. The image of mGO-ODA/MAPP-coated nylon film is shown in the Supplementary Information (Fig. S1).

2.4. Preparation of the composite-coated steel substrate for electrochemical corrosion studies

A measured amount of uniform composite solution was coated on polished and cleaned steel substrate (SS; 3 × 3 cm²), using a spray gun at 50 °C to prepare mGO-ODA/MAPP film coated on SS. The mGO-ODA/MAPP composite solutions (15% mGO-ODA/MAPP, 30% mGO-ODA/MAPP, 45% mGO-ODA/MAPP, and 60% mGO-ODA/MAPP) were prepared by mixing different amounts of mGO-ODA solutions (0.54 mL, 1.08 mL, 1.62 mL and 2.16 mL) into MAPP (18 mg in 1.5 mL of EC) solutions, according to the above preparation method (see Section 2.3). The samples were dried under air flow. Then, composite-coated steel substrates were dried in a vacuum oven at 60 °C for 12 h, to achieve dryness and good coating performance. The prepared test specimens were used as the working electrode for the electrochemical corrosion studies. The amounts of mGO-ODA in 15% mGO-ODA/MAPP, 30% mGO-ODA/MAPP, 45% mGO-ODA/MAPP, and 60% mGO-ODA/MAPP were 2.7, 5.4, 8.1, and 10.8 mg, respectively. The designations of these films for corrsion studies were similar to the gas barrier films. This is due to the fact that wt% of the filler with respect to the MAPP was similar for the both studies. Probable schematic representation of the interactions between mGO-ODA and MAPP, and coating of mGO-ODA/MAPP on a substrate (nylon or steel) are shown in Fig. 1.

2.5. Characterization

Ultraviolet-Visible (UV–Vis) spectroscopy at room temperature of mGO-ODA was performed using a UVS-2100 spectrophotometer (Scinco, Korea). Raman spectra of GO and mGO-ODA were obtained by Nanofinder 30 (Tokyo Instruments Co., Osaka, Japan). Thermogravimetric analyses (TGA) of all materials were performed under nitrogen atmosphere by Q50 TGA (TA Instruments, New Castle, US) with a heating rate of 5 °C/min. Fourier transform infrared (FTIR) spectroscopy and FTIR spectroscopy in an attenuated total reflection (ATR) mode (FTIR-ATR) were performed by Nicolet 6700 spectrometry (Thermoscientific, USA), in the wave number range of 4000–500 cm⁻¹. Wide angle X-ray scattering (WAXS) analysis was carried out on a D/Max 2500 V/PC (Rigaku Corporation, Japan) at ambient temperature at a scan rate of 2 °C/min. Atomic Force Microscope (AFM) experiment of mGO-ODA was prepared by casting a drop of mGO-ODA (0.01%, w/v) solution on polished silicon wafer. Transmission electron microscopy (TEM) measurements of mGO-ODA was done by JEM2200FS (Jeol, Japan) microscopy at 120 kV in the Jeonju center of KBSI. X-ray

photoelectron spectroscopy (XPS) of mGO-ODA was carried out by Theta Probe Instrument (Thermo Fisher Scientific, UK). The composite-coated nylon films were cut with a razor blade to observe the attachment between the coating layer and nylon film for cross-sectional field emission scanning electron microscopy (FESEM) analyses. The cross-sectional FESEM analyses of mGO-ODA/MAPP-coated nylon films were carried out by sputtering osmium prior to examination by FESEM (JSM-6701 Jeol, Japan). The fractured surface morphology of the composite films were examined using field emission scanning electron microscopy (FESEM; JSM-6701F, JEOL, Japan), and the cryogenic fracturing method was used to prepare the fracture surface of specimen by placing them in liquid nitrogen for 5 min. The fractured surface morphologies of these composites were also carried out by osmium puttering over the specimen surface. Tensile strength test of the nanocomposite films was performed on a universal testing machine (Instron model 5567 A, USA). Tensile strength was determined using the testing machine with a 2.5 kN load cell with an extension rate of 10 mm/min and gauge length of 30 mm. Pure nylon films with a thickness around 0.08 mm used during the coating of composite for mechanical study. The H_2 and O_2 gas transmission rate values of pure nylon sheet, MAPP-coated, mGO-ODA-coated, and mGO-ODA/MAPP coated nylon sheets were measured by GDP-C (Brugger Feinmechanik GmbH) gas permeability machine at 100 kPa (pressure) and 25 °C. The prepared films (the 2.5 cm-diameter test area of the sample) for the gas transmission rate (GTR) measurement were free of dust and completely free of grease. The GDP-C software provides the plot between the GTR and time. The GTR value was calculated from the software generated plot. To determine the GTR exactly, during evacuation residual gases and humidity has to be removed from the sample. The evacuation period and test period were used for 3 and 4 h respectively. The test gas must permeate upon initialization of the measurement phase. During this phase, the GTR value continuously increases. This value might decrease later due to solution processes inside the sample. After equilibration between the two processes, the GTR value remains constant and can be determined. The permeability coefficient value (P_1) of the coating layers on nylon film for different gases was calculated using Henis and Tripodi resistance model as follows [35,36]:

$$\frac{J}{\Delta p} = \frac{P}{l} = \left(\frac{l_1}{P_1} + \frac{l_2}{P_2} \right)^{-1}$$

where $J/\Delta p$, P, l are the permeation rate per pressure difference across the composite-coated sheet (GTR), the total permeability of the coated nylon sheet, and the total thickness of the coated nylon sheet, respectively. The l_1 and l_2 are thicknesses of the coating layer and the nylon, respectively. The permeability of pure nylon film for different gases was designated as P_2. More details regarding permeability coefficient calculations are provided in the Supplementary Information.

The electrochemical impedance spectroscopy (EIS) and potentiodynamic polarization measurements of coated specimens were done using a CH660D electrochemical workstation. The saturated Ag/AgCl, Cl⁻, platinum foil, and composite coated steel specimens served as reference electrode, counter electrode, and working electrode, respectively, in electrochemical corrosion cell. The electrochemical corrosion measurement was done in 3.5 wt% NaCl aqueous solution (corrosive medium). The potentiodynamic polarization analyses were scanned from cathodic to the anodic direction with a scan rate of 10 mV s⁻¹. Corrosion potential (E_{corr}), and corrosion current density (I_{corr}) were determined from the Tafel fitting of the polarization curve, and the corrosion rate (CR) was determined in mm/year. The working electrode was placed in the test environment for 30 min, before impedance measurements were taken. The EIS analyses of coated steel specimens was performed at their respective open circuit potential (OCP), and the measurements were conducted over a frequency range of 10⁵ to 10⁻¹ Hz with a signal amplitude of 5 mV. The measurements of all samples were repeated at least three times to ensure consistency.
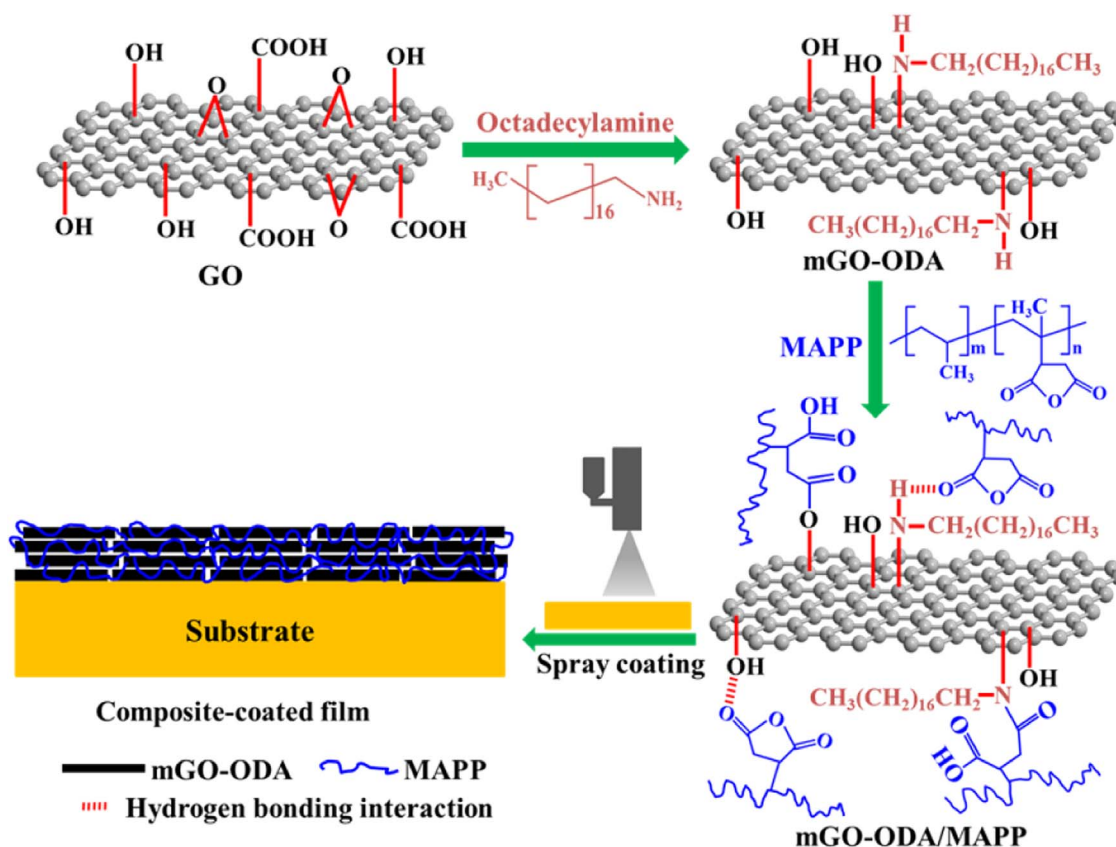
Fig. 1. Probable schematic representation of the interactions between mGO-ODA and MAPP and coating of mGO-ODA/MAPP on a substrate (nylon or steel).

3. Results and discussion

3.1. UV–vis spectra analysis

The ODA-modified reduced graphene oxide nanosheets (mGO-ODA) were well dispersed in different organic solvents (chloroform, cyclohexane, EC, etc.), and form stable black color dispersions. The presence of the long $CH_3(CH_2)_{16}CH_2$- (octadecyl chain) moiety changes the hydrophilic GO to hydrophobic mGO-ODA and improves the dispersibility of mGO-ODA in different organic solvents [26]. Fig. S2a shows the UV–vis spectra of mGO-ODA at different concentrations in EC. A linear relationship was found between the absorbance at 275 nm and the concentration (mg/mL) of mGO-ODA, as shown in the inset of Fig. S2a, suggesting the validity of Beer's law. The molar absorptivity (ε) of the mGO-ODA dispersion in EC was determined from the slope of the straight line. The ε value was found to be 36 mL mg^{-1} cm^{-1}. The ε value of mGO-ODA matches well with the alkylamine functionalized rGO reported in literature [2,37].

3.2. Raman spectra analysis

Fig. S2b depicts the Raman spectra of GO and mGO-ODA. The D band and G band of GO showed two salient peaks at 1354 cm^{-1} and 1566 cm^{-1}, respectively. The I_D/I_G values of GO and mGO-ODA were 0.94 and 1.05, respectively. The higher I_D/I_G value of mGO-ODA signifies the improved graphitization and removal of oxygenated groups from the surface of mGO-ODA [32]. The simultaneous functionalization and reduction of GO can generate a huge number of sp^2 domains (graphitic domains) with smaller size in mGO-ODA than GO [38,39]. The higher I_D/I_G value of mGO-ODA also indicates the high extent of the functionalization reaction, i.e., the presence of sp^3 defects within the sp^2 carbon network of mGO-ODA [25]. Raman spectrum of mGO-ODA confirmed simultaneous functionalization and reduction of GO by

ODA.

3.3. X-ray photoelectron spectroscopy analysis

X-ray photoelectron spectroscopy (XPS) was used to investigate the chemical reduction and functionalization of GO by ODA. The XPS survey scan results of GO showed that intensity of the oxygen peak is higher than the carbon peak, indicating a substantial oxidation of the graphite (Fig. 2a). The presence of an intense N 1 s peak at 398.8 eV in the survey spectrum of mGO-ODA confirmed the efficient functionalization of GO by ODA through > C–NH–C < bond formation. Besides, the survey spectrum of mGO-ODA showed less intense oxygen peak than carbon peak which suggested the successful reduction of GO by ODA [32,40]. Typically, the C 1 s peak region of GO can be deconvoluted into four curves (Fig. 2b). The binding energies at 284.8, 286.7, 287.2 and 289.4 eV are allocated to C—C/C=C, C–OH, C–O–C–, and –O–C=O bonds, respectively [26]. In the XPS spectrum of mGO-ODA, the peak intensities corresponding to oxygenated groups were prominently reduced than C–C/C=C peak. Fig. 2c shows a new peak at 285.4 eV corresponding to C–N bond, demonstrating the nucleophilic addition reaction between ODA and GO [28]. The deconvoluted N 1 s spectrum of mGO-ODA can be fitted into three curves that correspond to N–C (399.5 eV), N–C(O) (400.6 eV) and –NH$_3^+$–C (401.8 eV), respectively (Fig. 2d). The presence of –NH$_3^+$–C in N 1 s XPS supported the electrostatic interactions between ODA and GO.

3.4. AFM and TEM analyses

Fig. S3a and b show the AFM images of the mGO-ODA and GO, respectively. The thickness the mGO-ODA sheet was found to be 1.9 nm, which is higher than the thickness of single layer GO (about 1 nm). This is because of the attachment of large octadecyl group onto the GO surface of mGO-ODA [2]. The aspect ratio value (α) of the mGO-
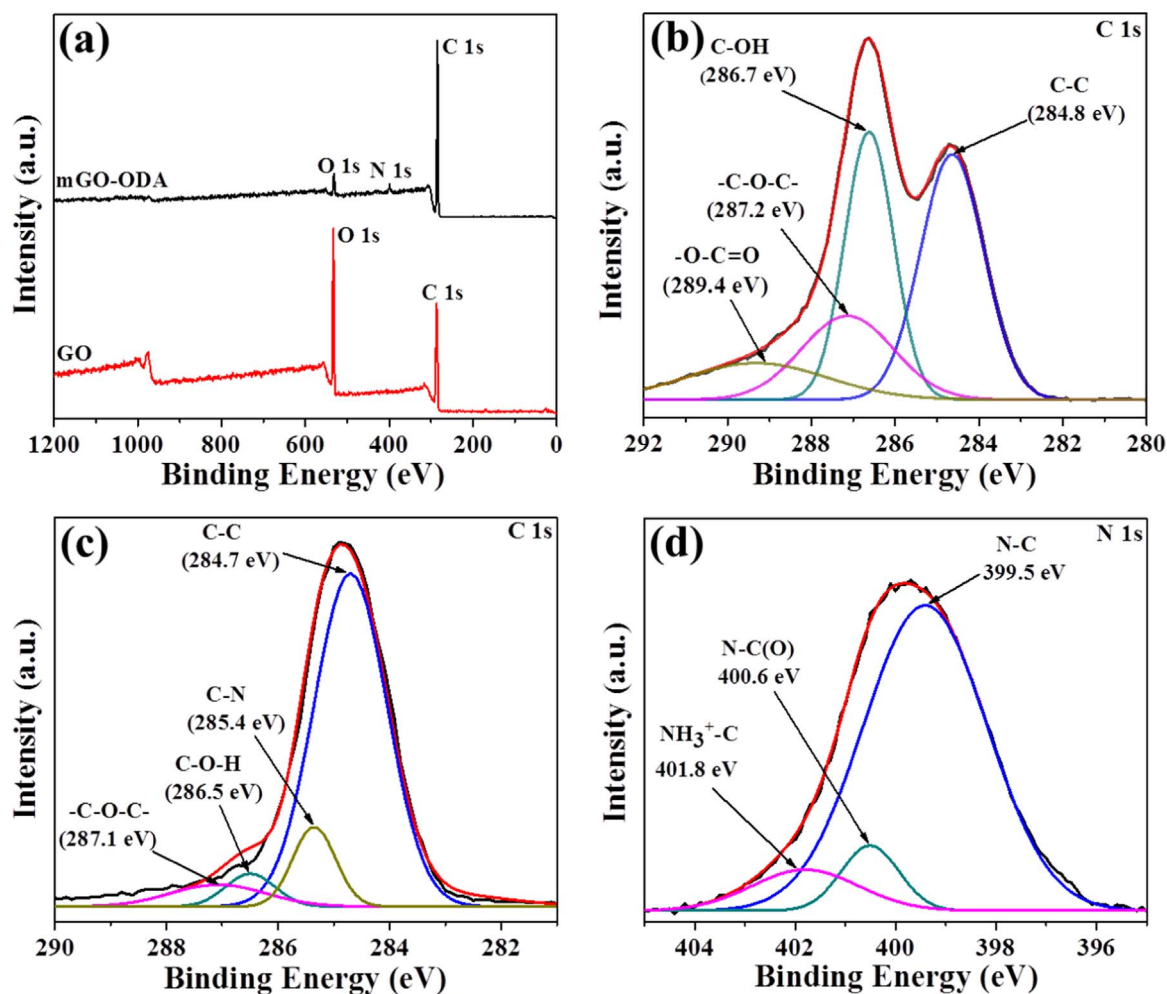
Fig. 2. XPS (a) survey spectra of GO, and mGO-ODA (b) C 1s of GO, (c) C 1s of mGO-ODA, (d) N 1s of mGO-ODA.

ODA was calculated to be of 800. Fig. S3c-e show the TEM, HRTEM and SAED patterns of mGO-ODA. The TEM image mGO-ODA displayed a clean and transparent graphene sheet (Fig. S3c–d). Furthermore, the HRTEM image displays the formation of graphene with few layers (Fig. S3e). The SAED pattern reveals distinct diffraction spots, demonstrating the six-fold hexagonal symmetry of graphene (inset of Fig. S3e). The unequal intensity of the diffraction spots in the SAED image might be attributed to the presence of large alkyl moieties on the graphene surface.

3.5. FTIR analysis of mGO-ODA and mGO-ODA/MAPP

Fig. 3a shows the FTIR spectra of GO, ODA, and mGO-ODA. GO showed a broad absorption peak in the range of 3585–3243 cm^{-1} due to the stretching of a vast number of hydroxyl groups. The other absorption peaks of GO typically appeared at 1730, 1622 and 1054 cm^{-1}
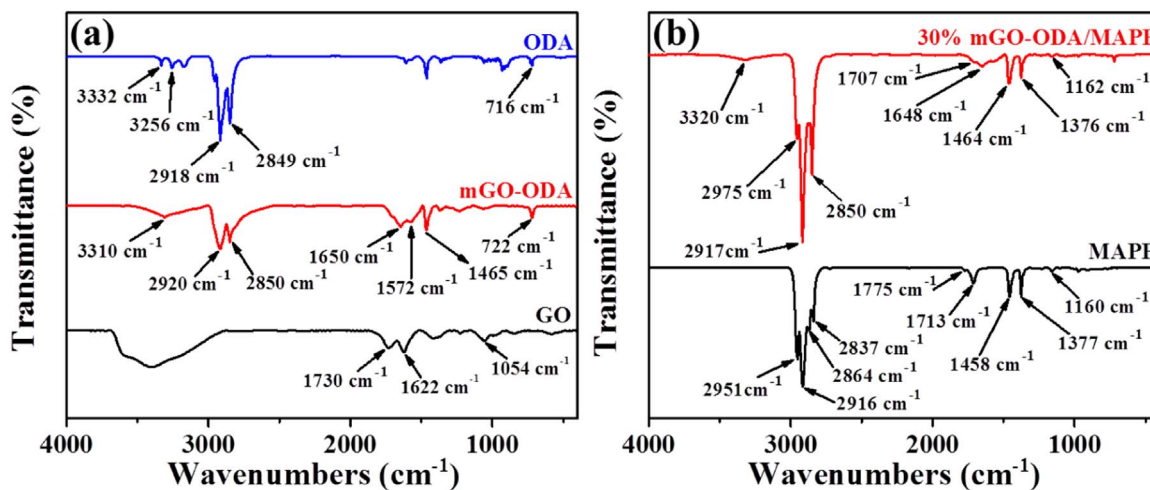

Fig. 3. (a) FTIR spectra of GO, mGO-ODA, and ODA, and (b) FTIR-ATR spectra of MAPP and 30% mGO-ODA/MAPP.

which correspond to the presence of > C=O stretching (carboxyl group), C–C stretching (C=C aromatic group), and C–O–C stretching (epoxy group) vibrations, respectively [14,26]. The asymmetric and symmetric stretching vibrations of the –CH$_2$– moiety of ODA chain appeared at 2920 and 2850 cm^{-1} respectively, demonstrating the presence of ODA moiety on the GO surface in mGO-ODA. The mGO-ODA exhibited new peaks at 1572 (N–H stretching vibration), and 1465 cm^{-1} (C–N stretching vibration) which indicate the formation of –C–NH–C– bonds [2,26,37]. The functionalization reaction of GO by ODA was also confirmed by the absence of the two characteristic peaks of the amine group of ODA at 3332 and 3256 cm^{-1}, and by the appearance of a broad peak at 3310 cm^{-1} for mGO-ODA [26]. Fig. 3b shows the FTIR-ATR spectra of MAPP and 30% mGO-ODA/MAPP. MAPP exhibited absorption peaks for asymmetric stretching of –CH$_3$ group (2951 cm^{-1}), symmetric stretching of –CH$_2$ group (2916 cm^{-1}), symmetric stretching of –CH$_3$ group (2864 cm^{-1}), and symmetric stretching of –CH$_2$ group (2837 cm^{-1}). Besides, MAPP also exhibited characteristic absorption bands at 1775 and 1713 cm^{-1} (–C=O stretching bands of maleic anhydride), 1458 cm^{-1} (asymmetric C–H bending vibration of –CH$_2$ and –CH$_3$ groups), 1377 cm^{-1} (symmetric C–H bending vibration of –CH$_2$ and –CH$_3$ groups), 1160 cm^{-1} (stretching of C–C bond of C–CH$_3$ group) [28,29]. The FTIR-ATR spectra of MAPP and mGO-ODA/MAPP did not show significant difference in their peak intensity and peak position. The mGO-ODA/MAPP showed a new peak at 3320 cm^{-1} corresponding to the stretching N–H bonds, suggesting the chemical interactions between mGO-ODA and MAPP (Fig. 1) [27]. Besides, the mGO-ODA/MAPP also showed an intense peak at 1648 cm^{-1} which indicate the formation of amide linkage between mGO-ODA and MAPP [25,28].

3.6. XRD studies of mGO-ODA and mGO-ODA/MAPP

The typical diffraction peak (002) of GO was found at approximately $2\theta = 11.9°$, and interlayer spacing (d$_{sp}$) corresponding to this peak is 0.75 nm (Fig. 4a). In comparison to GO, the d$_{sp}$ of mGO-ODA was further enlarged to 1.13 nm, with a 2θ value of 7.9°, signifying that ODA molecules were covalently inserted with GO sheets. In addition, the XRD pattern of mGO-ODA exhibited one broad peak at approximately 21.1°, indicating the restoration of the graphitic structure. The long octadecyl chain can detain the restacking of graphene sheets; therefore, mGO-ODA sheets are inadequately arranged along the different stacking directions, resulting in a broad peak at larger 2θ value [41,42]. Fig. 4b shows the of crystalline phases of MAPP that are confirmed by the appearance of peaks (2θ) at 13.7°, 15.8°, 17.6°, 19.5°, 21.1° and 28.8° corresponding to 110, 040, 130, 111, 131 + 041, 220 crystalline phases, respectively [28,43]. MAPP and mGO-ODA/MAPP composites exhibited similar diffraction patterns in the XRD as shown in Fig. 4b. In the diffraction pattern of the composites, only crystalline diffraction peaks of MAPP have been observed, indicating that most of the mGO-ODA nanosheets were finely exfoliated and dispersed in the MAPP matrix. It is important to mention that the peaks for mGO-ODA could not found in the XRD spectra of the composites. These results coincide with those found for PP/graphene composites, as reported by several literatures [28,43].

3.7. Thermogravimetric analysis

TGA analysis of mGO-ODA also revealed functionalization and reduction of GO by ODA. The initial weight loss of GO below 100 °C is due to the evaporation of water between the GO sheets (Fig. 4c) [2,40]. Besides, GO exhibited a significant weight loss in the range of 140–250 °C, resulting from the exclusion of oxygenated functional groups from the GO surface. ODA exhibited low thermal stability, and almost decomposed within 300 °C. For the long alkyl chain containing monoamine modified rGO, thermal degradation of the oxygenated groups, alkylated chains, and the carbon skeleton occur in the range of

120–550 °C [2,37]. The mGO-ODA displayed very less weight loss up to 140 °C, suggesting the more hydrophobic nature of mGO-ODA compared to GO, as shown in Fig. 4c. However, mGO-ODA showed a mass loss of about 4 wt% in the temperature range of 160–210 °C, which is attributed to the physically adsorbed ODA. At higher temperature, the mass loss of mGO-ODA can be attributed to the chemically bonded ODA in mGO-ODA. The TGA data suggested that the mGO-ODA contained around 30% covalently bonded ODA molecules in mGO-ODA. Li et al. and Yang et al. also reported similar type TGA curves for alkylamine modified GO [26,37]. Fig. 4d shows TGA curves of pure MAPP and mGO-ODA/MAPP composites under nitrogen atmosphere. Initially (from 150 to 410 °C), the composites showed lower thermal stability than MAPP. This is due to the degradation of octadecyl group from mGO-ODA of mGO-ODA/MAPP composite. The final degradation temperatures (after 413 °C) of the composites (30% mGO-ODA/MAPP, and 60% mGO-ODA/MAPP) were much higher than that of neat MAPP. The 70% weight loss temperatures of MAPP, 30% mGO-ODA/MAPP, and 60% mGO-ODA/MAPP were 448, 458, and 460 °C, respectively. The enhanced thermal stability of the composites are attributed to the barrier role of the mGO-ODA sheets, which inhibit the permeation of small gaseous molecules during thermal degradation [44,45]. Besides, the improvement in thermal stability of the composite is also attributed to the homogeneous dispersion of the mGO-ODA sheets in the MAPP polymer matrix.

3.8. FESEM analysis

The fractured surface cross-sectional FESEM images of the pure MAPP and composite films (Fig. 5) were studied to examine and compare their morphologies. The fractured surface of pure MAPP was very smooth and uniform, while all these composites showed rough surface. In comparison to MAPP, the rough surfaces of the composites indicated that tight attachment of the mGO-ODA with MAPP and higher energy absorbed during fracture [25,27,37]. However, large mGO-ODA nanosheets with a wrinkled morphology can be clearly seen in the nanocomposites, suggesting that the mGO-ODA has excellent interaction with MAPP (Fig. 5b–e) [27]. It can be stated that mGO-ODA is a perfect choice as nanofiller to reinforce the MAPP.

Besides, the cross-sectional FESEM analyses of the composite coated nylon films have been performed to understand the structure of the coating layer and examine the attachment of the mGO-ODA/MAPP on the nylon sheet (Fig. 6a–d). The cross-sectional FESEM of mGO-ODA-coated nylon film is shown in Fig. S4. The thicknesses of different mGO-ODA/MAPP composite coated samples were measured from the cross-sectional FESEM imagery, and thicknesses values are provided in Table S1. The cross-sectional FESEM images indicated highly packed structure of the coating layer. Maleic anhydride moiety of MAPP undergoes hydrogen bonding interaction or chemical interaction with the terminal groups of modified nylon, resulting in excellent attachment between MAPP and nylon film. Thicker graphene sheets were formed by increasing the loading of fillers in their corresponding composites. 60% mGO-ODA/MAPP showed highest thickness in this series.

3.9. Mechanical properties

Fig. 7a presents the typical tensile stress-strain curves of the different types of mGO-ODA/MAPP nanocomposites-coated, MAPP-coated and pure modified nylon films. Fig. 7b represents the elastic modulus (E) of all composite films. The MAPP-coated film exhibited higher tensile strength and E value compared to pure nylon film, suggesting that MAPP (adhesive) properly attached with nylon film and improved the mechanical property of nylon. The presence maleic anhydride moiety helps to bind MAPP with modified nylon surface efficiently. All these mGO-ODA/MAPP composite films showed higher tensile strength and E values than the MAPP-coated and pure nylon films, suggesting the formation of mechanically durable composites. The trend in the
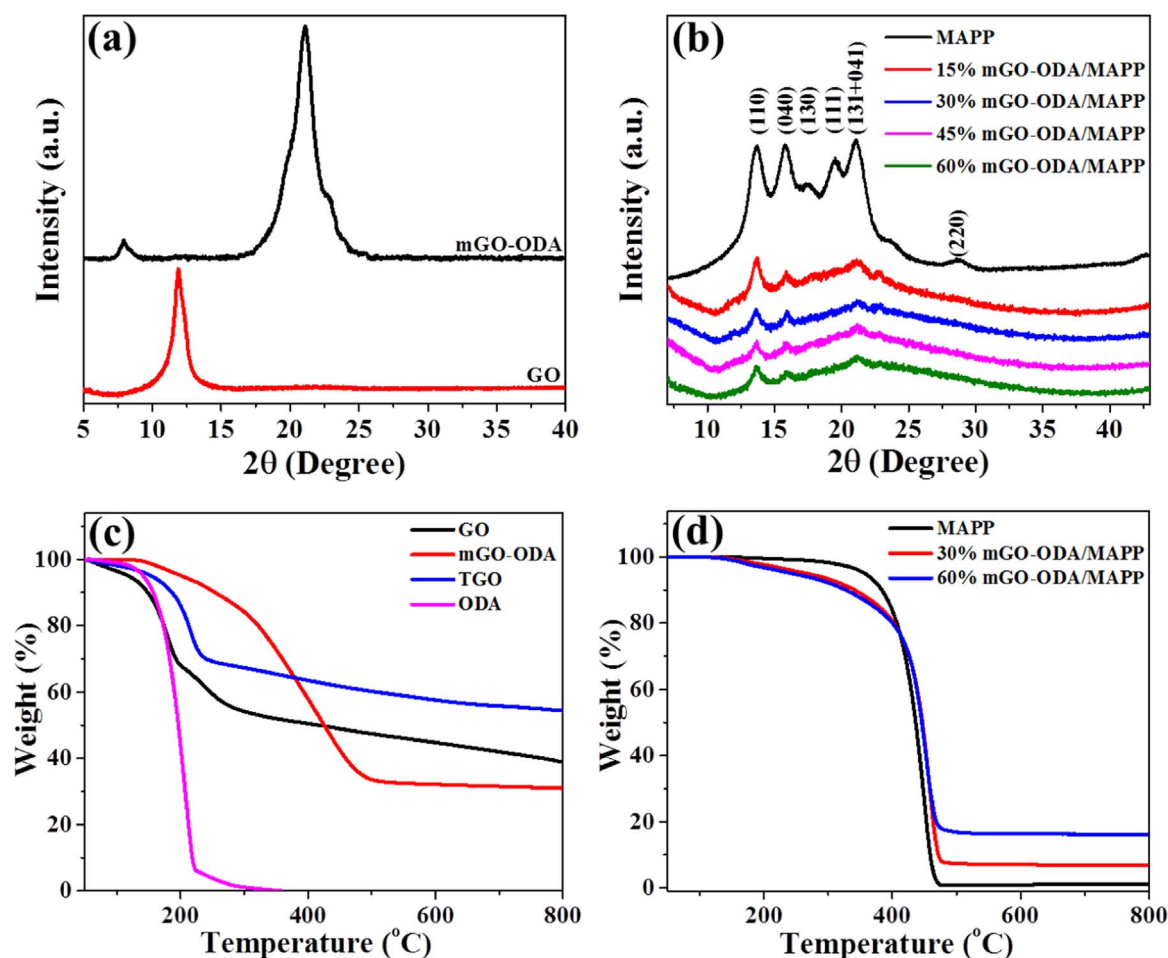
Fig. 4. XRD patterns of (a) GO and mGO-ODA, (b) MAPP and mGO-ODA/MAPP composites, and TGA curves of (c) GO, mGO-ODA, TGO and ODA, and (d) MAPP, 30% mGO-ODA/MAPP, and 60% mGO-ODA/MAPP.

mechanical property of these nanocomposite films was similar to the graphene-based isotactic polypropylene nanocomposites [28]. ODA functionalized-graphene/low density polyethylene nanocomposites also showed similar trend in mechanical property [37]. The improved mechanical properties of these composites are due to the addition mGO-ODA as reinforcing filler. The excellent dispersion of mGO-ODA within MAPP matrix as well as strong interfacial interactions between them improves the mechanical property of the composite-coated film. The polar maleic anhydride moiety of MAPP undergoes hydrogen bonding interaction with the mGO-ODA; besides, maleic anhydride moiety of MAPP is very reactive towards hydroxyl group and amine groups. Therefore, mGO-ODA having hydroxyl group and amine groups undergoes excellent interfacial interaction with the MAPP in mGO-ODA/MAPP composites. The tensile strength and E of the composite films increased with the increase in mGO-ODA loading and 60% mGO-ODA/MAPP-coated nylon film showed highest tensile strength and E values. The E values of 60% mGO-ODA/MAPP-coated, MAPP-coated, and pure nylon films were found to be 343, 178 and 162 MPa, respectively. Therefore, 93% and 112% enhancements in E values of 60% mGO-ODA/MAPP–coated nylon film in comparison to MAPP-coated and pure nylon signify that mGO-ODA reinforces MAPP. Figs. 5 and 6 show the morphologies which conferred higher mechanical property of these composite-coated nylon films. Graphene-reinforced nylon-6 composites also showed similar trend in mechanical property compared to pure nylon 6 [46]. The improvement in E value is much smaller for glassy polymer based graphene composite. However higher modulus and high aspect ratio (800) of mGO-ODA help to improve the mechanical properties of the composites-coated nylon films.

3.10. Gas barrier properties of mGO-ODA/MAPP composite-coated nylon films

H_2 gas transmission rates (H_2GTR) and O_2 gas transmission rates (O_2GTR) of pure nylon, MAPP-coated and composite-coated nylon films were measured at 25 °C and 100 kPa. Fig. 8 and Table S1 demonstrate the H_2GTR and O_2GTR values of pure nylon, MAPP, mGO-ODA and mGO-ODA/MAPP composite-coated nylon films. H_2 has lower kinetic diameter than O_2; therefore, the H_2GTR values of all these films are higher than that of O_2GTR. Pure nylon film exhibited H_2GTR and O_2GTR values of 180 and 40 cc m^{-2} day^{-1} atm^{-1}, respectively (Fig. 8a–b). In comparison to the pure nylon film, H_2GTR and O_2GTR values reduced significantly in the mGO-ODA/MAPP-coated nylon films. The 60% mGO-ODA/MAPP film showed lowest H_2GTR and O_2GTR values of 10.6 and 2 cc m^{-2} d^{-1} atm^{-1}, respectively. The permeability coefficient (P_1) values for H_2 (P_{1H2}) and O_2 (P_{1O2}) gases of these coating layers (MAPP, mGO-ODA and mGO-ODA/MAPP) deposited on nylon films were evaluated by the Henis and Tripodi resistance model (Supplementary Information) and these values are presented in Fig. 8 and Table S1 [2,35,36]. The P_{1H2} and P_{1O2} values of 60% mGO-ODA/MAPP-coated nylon film were calculated to be 0.259 and 0.049 cc mm m^{-2} d^{-1} atm^{-1}, respectively. The pure mGO-ODA-coated nylon film (same loading of mGO-ODA as 30% mGO-ODA/MAPP) showed H_2GTR and O_2GTR values of 51.1 and 19 cc m^{-2} d^{-1} atm^{-1}, respectively. The 30% mGO-ODA/MAPP exhibited lower GTR values for H_2 and O_2 gases compared to only 30% mGO-ODA-coated nylon films. MAPP (adhesive) can increase the adhesion of the mGO-ODA/MAPP composite onto the modified nylon surface. Therefore,
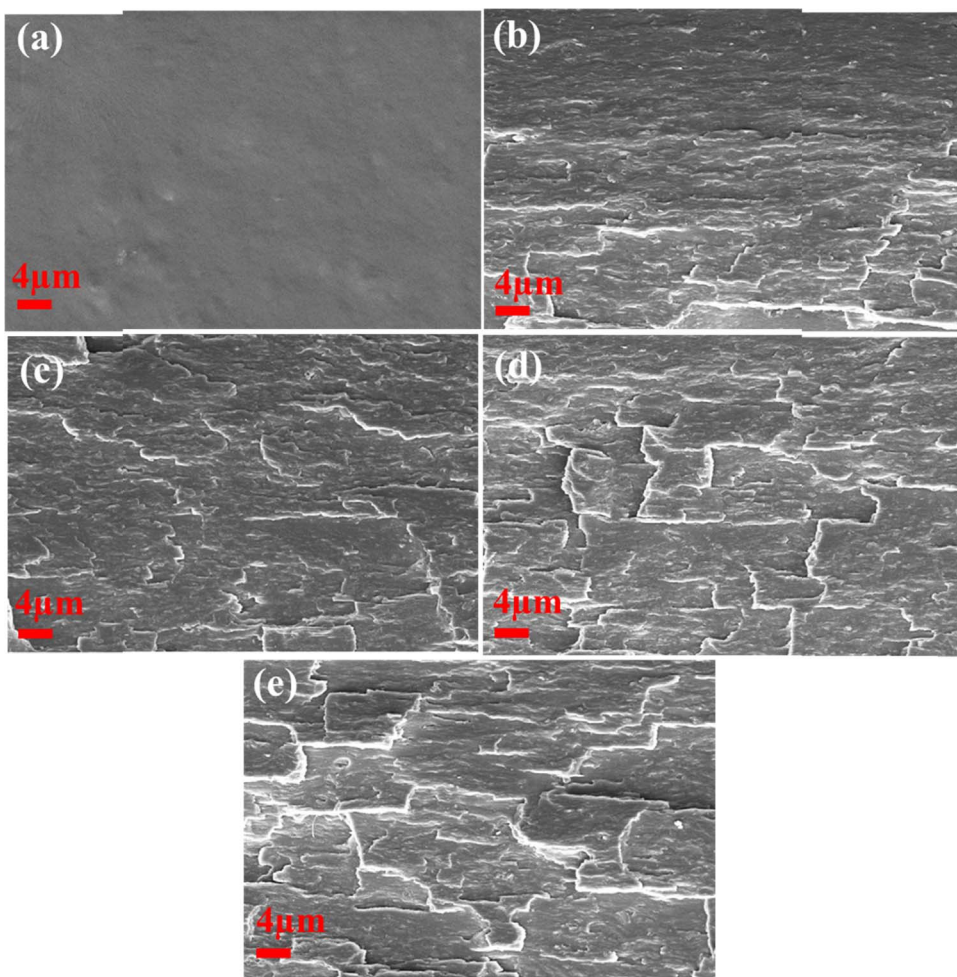
Fig. 5. FESEM images of the fractured surfaces of (a) pure MAPP, (b) 15% mGO-ODA/MAPP, (c) 30% mGO-ODA/MAPP, (d) 45% mGO-ODA/MAPP, and (e) 60% mGO-ODA/MAPP.

mGO-ODA/MAPP composite coated nylon films exhibited much lower GTR values, compared to the mGO-ODA coated nylon film. The 60% mGO-ODA/MAPP-coated nylon film exhibited 80% and 90% reduction in H_2GTR and O_2GTR values compared to MAPP (50 mg) coated nylon film (Table S1). The octadecyl chains can wrap up the graphene sheets completely; therefore, ODA can minimize the defects and nanochannels in mGO-ODA sheets [2]. The hydrogen bonding interaction between mGO-ODA and MAPP provides strong interfacial interaction between
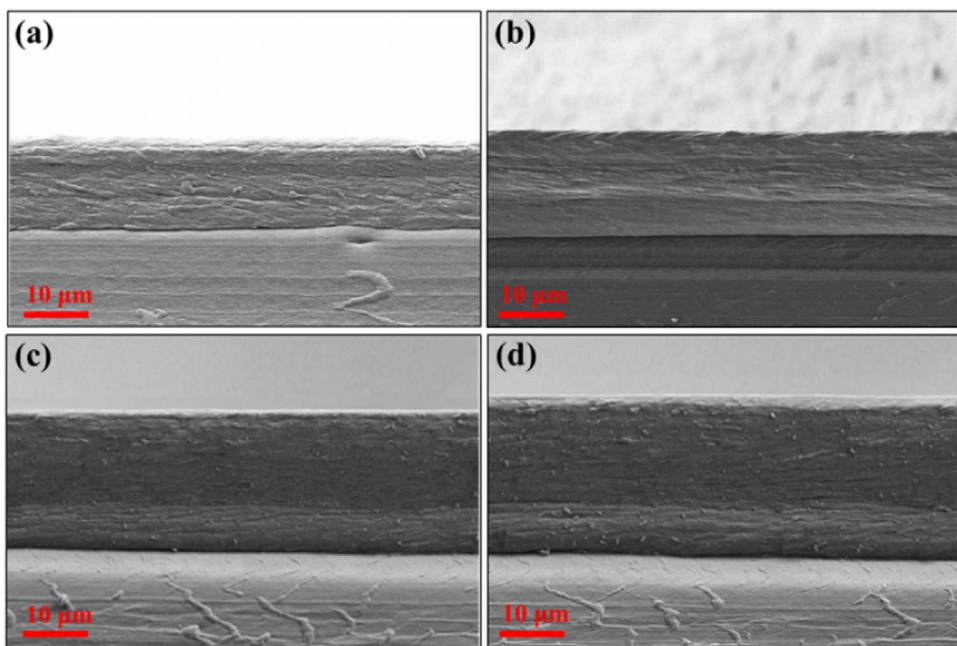

Fig. 6. Cross-sectional FESEM images of (a) 15% mGO-ODA/MAPP, (b) 30% mGO-ODA/MAPP, (c) 45% mGO-ODA/MAPP, and (d) 60% mGO-ODA/MAPP-coated nylon films.
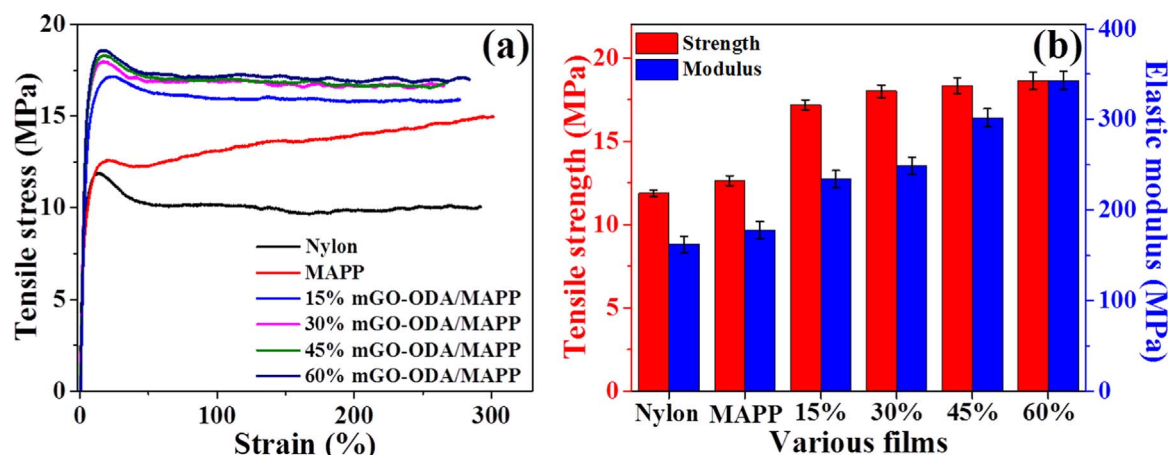
Fig. 7. (a) Typical tensile stress-strain curves and (b) summary of tensile strength and elastic modulus data of the nanocomposite-coated, MAPP-coated, and pure nylon films.

them. Besides maleic anhydride moiety of MAPP is very reactive towards hydroxyl and amine moiety of mGO-ODA. Therefore, there might be an effective interfacial load transfer between mGO-ODA and MAPP, resulting in lesser fractional free volume (FFV) for the permeation of gas molecules in mGO-ODA/MAPP. The mGO-ODA sheets also densify the MAPP matrix and inhibit the mobility of polymer chain, resulting in lower FFV [2,6]. In other words, preferential alignment and very high aspect ratio (800) of mGO-ODA sheets in the MAPP matrix hinder molecular diffusion of gases through these composite by forming the compacted gas barrier layer. Therefore, impermeable mGO-ODA sheets bound the gas molecules to travel through longer and more tortuous paths to pass through the composite coated nylon film, resulting in lower GTR value than the MAPP-coated and pure nylon film [1,40]. We have found that the gas barrier properties of the composite-coated films

were higher than or comparable to the reported graphene based composite-coated film (Table S2) [1,2,4,8,31,32,40,47–50]. The GTR and P_1 values of the mGO-ODA/MAPP-coated nylon films declined with the higher loading of mGO-ODA in MAPP. The higher mGO-ODA loading can creates more perfect dense gas barrier layer which produce an enormously long and more tortuous paths for the gas molecules. Therefore, GTR decreased significantly with the higher loading of graphene sheets. The 60% mGO-ODA/MAPP-coated film has the highest thickness of 23 μm and it produced the lowest GTR and P_1 value in this series for H_2 and O_2 gases.

In a semi-crystalline polymer, the impermeable crystalline phase inhibits the diffusion of gas molecules, and the gas molecules diffuse through the amorphous permeable phase [7,31]. Therefore, the barrier properties of mGO-ODA/MAPP-coated nylon film also depend to some
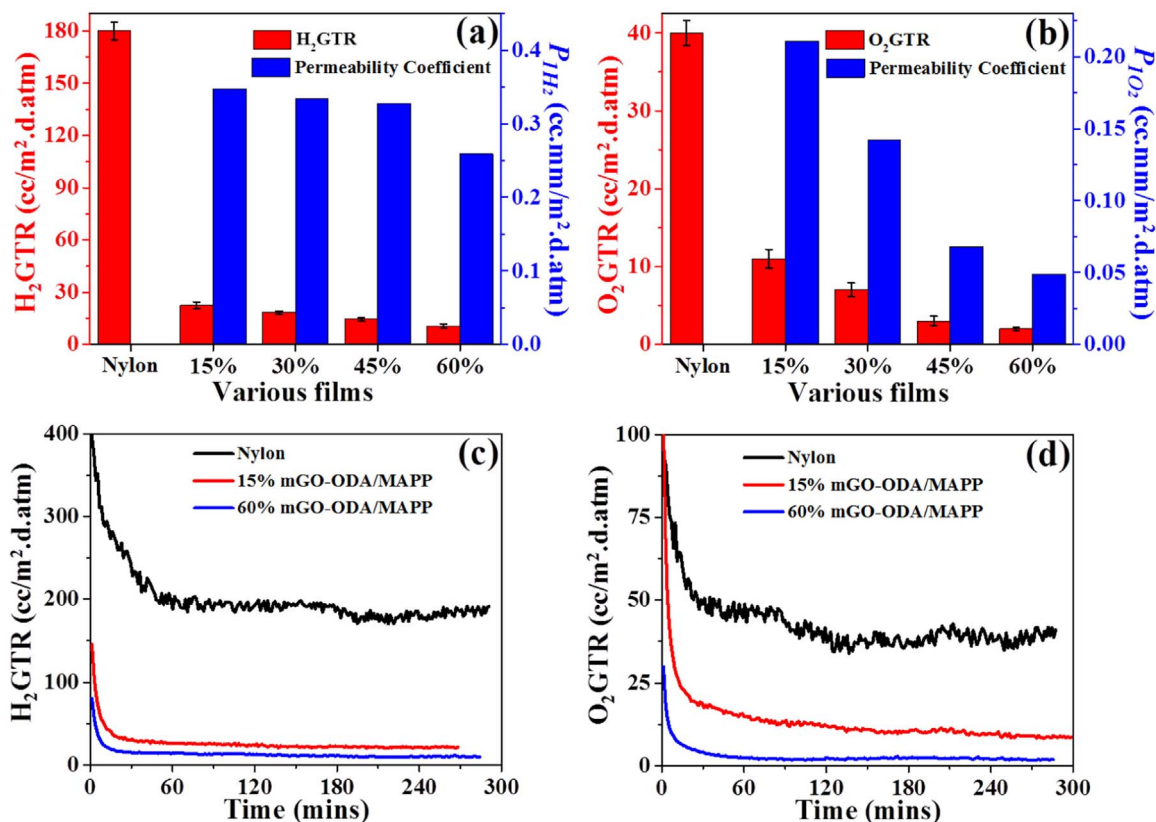

Fig. 8. (a) H_2GTR and permeability coefficient (P_{1H2}) values of H_2 gas, (b) O_2GTR and permeability coefficient (P_{1O2}) values of O_2 gas of all films, and the instrumental generated GTR plots of (c) H_2 and (d) O_2 gases for 15% mGO-ODA/MAPP and 60% mGO-ODA/MAPP composite-coated nylon films.
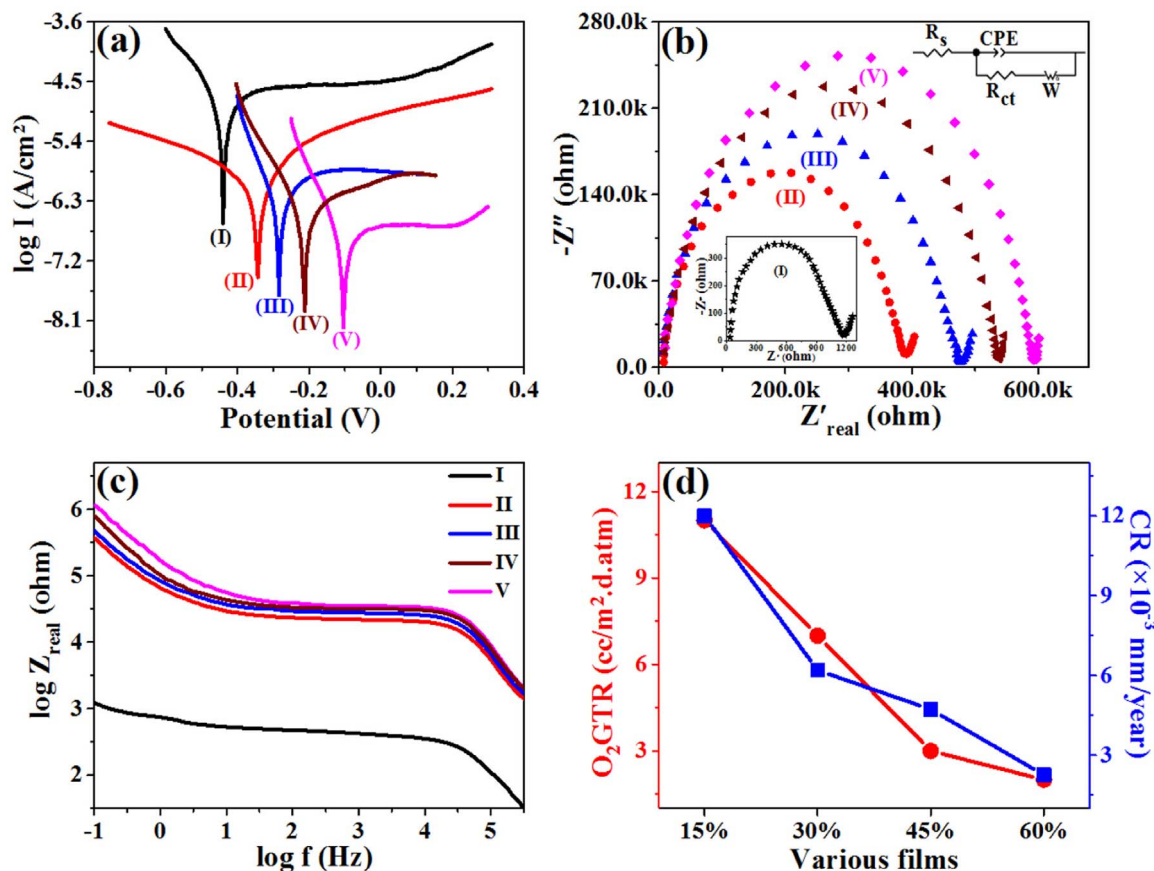
Fig. 9. (a) Tafel, (b) Nyquist, (c) Bode plots of SS (I), 15% mGO-ODA/MAPP (II), 30% mGO-ODA/MAPP (III), 45% mGO-ODA/MAPP (IV), and 60% mGO-ODA/MAPP (V), and (d) the plot of O_2GTR and corrosion rate values for all the composite-coated substrate.

extent on the crystallinity of the MAPP (Fig. 4b). The crystallites and crystalline regions inhibit the diffusion of gas molecules through the mGO-ODA/MAPP-coated nylon by increasing the tortuosity of the permeate path. Therefore, the crystallinity and crystalline region of MAPP have some role to improve the gas barrier properties of mGO-ODA/MAPP-coated nylon films. The mGO-ODA/MAPP composite can also form a brick wall type structure, where mGO-ODA and MAPP can act as the brick, and mortar, respectively. This type of structure can produce super tortuosity for the H_2 and O_2 gas molecules [31].

The tradeoff relationship (decrease of permeability accompanied by increase in permselectivity) was observed between permeability and permselectivity (H_2GTR/O_2GTR or P_{1H2}/P_{1O2}) of all the composite coated films with the increase of mGO-ODA loading in MAPP (Table S1). The highest amount of mGO-ODA in 60% mGO-ODA/MAPP can densify and rigidify the MAPP matrix most, resulting in highest permselectivity and lowest permeability. The highest tensile strength and elastic modulus values supports the formation of most dense and rigid coating layers for 60% mGO-ODA/MAPP-coated nylon film. Therefore, rotational mobility of MAPP chain greatly reduced in 60% mGO-ODA/MAPP-coated nylon film, resulting in highest permselectivity in this series.

The instrumental generated GTR plots of H_2 and O_2 gases are shown in Fig. 8c and d, respectively. These plots showed that GTR values were constant for almost 3 h. In other words, these films did not show any decrease in GTR value with time for long time duration. It can be stated that mGO-ODA/MAPP coatings can exhibit not only excellent barrier properties but also enhanced thermal stability and mechanical properties which are favorable for industrial applications.

3.11. Electrochemical corrosion properties of composite coated steel substrate

The mGO-ODA/MAPP coated nylon films showed excellent gas barrier properties toward H_2 and O_2. It is already reported that the presence of large alkyl group and formation of reduced graphene oxides improve the barrier properties towards water vapor. Therefore, mGO-ODA/MAPP could be used as a promising material for corrosion protection of stainless steel (SS). The adhesive strength of the coating was performed to evaluate the adhesion of composite on the steel (Fig. S5). The coating was scrawled into 2 mm × 2 mm girding by using a razor, and then the Scotch® Tape was pressed and dragged to remove it from the notched surface. The mGO-ODA/MAPP composite coated film showed excellent adhesion onto the steel surface with negligible peeling at the connection of the scratches after removing the tape. MAPP acts as adhesion promoter and helps to improve the adhesion between SS and composite. The corrosion protection efficiency of all the coated specimens was examined in 3.5 wt% NaCl aqueous solution and compared with steel. The corrosion current (I_{corr}) was determined from the Tafel polarization curve by extrapolating a straight line along the linear portion of the cathodic and anodic plot and extending these lines up to the E_{corr} axis to obtain the crossing point.

CR is the corrosion rate (mm/year), which was calculated using the following formula [20,21,51,52]:

$$CR = \frac{I_{corr}(A/cm^2) \cdot M(g)}{D(g/cm^3) \cdot V}$$

where, *V* is the valence, *M* is the molecular weight, 3270 is a constant, and *D* is the density.

The corrosion inhibition efficiencies (*IE%*) of the composite-coated steel substrate are calculated from the following equation:

$$IE\% = \frac{I_{corr,s} - I_{corr,c}}{I_{corr,s}}$$

where, $I_{corr,s}$ and $I_{corr,c}$ are the corrosion current of steel, and the coated specimen, respectively. The Tafel polarization curves of different coated-specimens are shown in Fig. 9a. The corrosion parameters (I_{corr}, E_{corr}, CR and IE%) are presented in Table S3. Tafel polarization curves show that composite-coated specimen displayed more positive E_{corr} values, compared to the bare steel. The polarization curves (hyperbolic plot) of the composite-coated specimen moved to the lesser current density with the increase of mGO-ODA loading, suggesting that the anticorrosion performance of composite improved with the higher loading of mGO-ODA. Table S3 shows that E_{corr} increases, while I_{corr} and CR decrease with higher mGO-ODA loading. It suggests that the coating of mGO-ODA/MAPP composite exhibits excellent corrosion protection for the SS. The CR of the 60% mGO-ODA/MAPP-coated sample showed a 119-fold reduction than the bare SS. All these mGO-ODA/MAPP-coated SS samples exhibited substantial improvements in IE% values compared to bare SS. The 60% mGO-ODA/MAPP composite exhibited highest IE% value of 99.15%. Based on the obtained corrosion parameters it is clear that mGO-ODA/MAPP showed improved or comparable anticorrosion properties than the reported polymer/graphene composites [14,19,20,22,53–55]. The long octadecyl chains in mGO-ODA can cover up defects in graphene and make graphene highly hydrophobic. The ODA moiety also inhibits the connectivity between graphene sheets. The hydrogen bonding interaction between MAPP and mGO-ODA improves the interaction between mGO-ODA and MAPP. Besides, the chemical reaction between maleic anhydride moiety of MAPP and mGO-ODA assist to bound mGO-ODA tightly and very efficiently with MAPP matrix. Therefore, mGO-ODA/MAPP composite can minimize the contacts between graphene and metal [13]. The corrosion behavior of mGO-ODA/MAPP composites was monitored and compared with SS by employing EIS analysis using 3.5 wt% NaCl aqueous solutions as an electrolyte (Fig. 9b). The inset of Fig. 9b displays the corresponding equivalent Randles circuit of all these Nyquist plots. Randles circuit parameters consist of solution resistance (R_s), constant phase element (CPE), charge-transfer resistance/polarization resistance (R_{ct}) and Warburg element (W). The diameter of the Nyquist Plot typically decreased with the lower polarization resistance or charge transfer resistance during the process of corrosion. The arc length of the semicircles increased in the order of steel < 15% mGO-ODA/MAPP < 30% mGO-ODA/MAPP < 45% mGO-ODA/MAPP < 60% mGO-ODA/MAPP. The above trend indicates that the charge transfer resistance increases with the higher loading of mGO-ODA in the polymer matrix. The charge transfer resistance of SS, 15% mGO-ODA/MAPP, 30% mGO-ODA/MAPP, 45% mGO-ODA/MAPP, and 60% mGO-ODA/MAPP-coated composites were 1.2, 385.4, 474.6, 530.9, and 590.4 kΩ/cm², respectively. The EIS plots of these composites are looks like perfect semicircles, indicating the single charge-transfer reaction and deviance from the perfect double-layer capacitor [14,53]. This is attributed to the lower conductivity between the electrolyte solution and coating layer. However, at low frequency, diffusion effects control corrosion process; thereby a Warburg impedance part (W) was incorporated in the circuit. Fig. 9c shows the Bode plots (impedance vs. frequency) for SS and coated specimens in 3.5 wt% NaCl solution, indicating impedance modulus. At the lowest frequency in Bode plots, the value of Z_{real} indicates the resistance of the coating material towards corrosion. In the Bode magnitude plots, at low frequency the values of Z_{real} follow the order as steel < 15% mGO-ODA/MAPP < 30% mGO-ODA/MAPP < 45% mGO-ODA/MAPP < 60% mGO-ODA/MAPP. At low frequency, the larger value of impedance modulus signifies a low I_{corr}. The above trend indicates that 60% mGO-ODA/MAPP exhibited best anticorrosion performance.

The corrosion protection efficiency of various polymer composites based on graphene can be explained by the gas barrier-improved mechanism [14,20]. In this study, the decreasing trend in GTR values

matches well with the decrease in corrosion rate of all the composites (Fig. 9d). Therefore we tried to explain the anticorrosion performance by gas barrier-improved mechanism. The occurrence of corrosion and rust formation on SS comprises several steps (oxidation and reduction reactions). The H_2O and O_2 are needed for the development of corrosion on the steel surface. The anodic process involves dissolution of Fe, and cathodic process involves formation of OH^- during corrosion. Increasing the tortuosity of the diffusion pathways through the composite can efficiently prevent the contact of H_2O and O_2 on the steel surface, leading to an excellent anticorrosion property. Hydrogen bonding and chemical interaction between MAPP and mGO-ODA help to achieve good dispersion and well exfoliation of mGO-ODA in MAPP matrix. The flexible and very high aspect ratio (800) mGO-ODA sheets could considerably increase the tortuosity of the diffusion pathways for O_2, Cl^- and H_2O, inhibiting the corrosion reaction from arising in the interface between the composite and the steel surface. The films formed by mGO-ODA/MAPP composite coatings on the nylon and SS surfaces were highly competent to improve gas barrier and anticorrosion performances, respectively. Therefore, the as-prepared composite can be successfully utilized to make hydrogen storage apparatus for fuel cell, barrier material for food packaging and anticorrosion coating.

4. Conclusion

The ODA simultaneously reduces and functionalizes hydrophilic GO to hydrophobic mGO-ODA in a one-step method without the use of toxic reducing agents. The mGO-ODA sheets form a more homogeneous and stable dispersion in non-polar solvents (e.g., chloroform, cyclohexane, and EC) without degradation of size and shape, in comparison to the polar hydrophobic solvents. TGA, FTIR, Raman and XPS spectroscopy analyses confirmed functionalization and reduction of GO to mGO-ODA. According to the AFM image analysis, the average thickness and aspect ratio of mGO-ODA were 1.9 μm and 800, respectively. A series of mGO-ODA/MAPP composites were prepared by mixing different amounts of mGO-ODA with a fixed amount of MAPP to examine their applicability as the gas barrier and anticorrosion coating materials. FTIR analysis confirmed that the chemical interaction between MAPP and mGO-ODA. The XRD analysis confirmed that mGO-ODA nanosheets were finely exfoliated and dispersed in the MAPP matrix. The rough surfaces of the composites in comparison to MAPP indicated that higher energy absorbed during fracture. Super hydrogen and oxygen barrier films were fabricated by spray coating of mGO-ODA/MAPP composites on modified nylon surface. Cross-sectional FESEM analyses of the coated films indicated good attachment between the composites and the nylon surface. The chemical surface modification of nylon surfaces has been accomplished by reaction at the terminal amine or carboxylic acid group or at the repeating amide group. Maleic anhydride moiety of MAPP undergoes hydrogen bonding interaction and chemical interaction with these terminal groups of modified nylon, resulting in excellent adhesion between MAPP and nylon film. All these mGO-ODA/MAPP-coated nylon films exhibited excellent improvement in mechanical and gas barrier properties compared to MAPP-coated and pure nylon films. The thermal stability, gas barrier and mechanical properties dramatically improved with the increase of mGO-ODA loading in MAPP. The elastic modulus values of 60% mGO-ODA/MAPP-coated nylon film (highest mGO-ODA loading) was found to be 343 MPa. The H_2GTR and O_2GTR values of 60% mGO-ODA/MAPP-coated nylon films were 10.6 and 2 cc m^{-2} day^{-1} atm^{-1}, respectively, as compared to the H_2GTR and O_2GTR values of nylons were 180 and 40 cc m^{-2} day^{-1} atm^{-1}, respectively. Besides, mGO-ODA/MAPP-coated steel substrates exhibited excellent anticorrosion properties in a 3.5 wt% NaCl electrolyte solution. The mGO-ODA/MAPP composites showed excellent improvements in anticorrosion performance with the increase of mGO-ODA loading. The lowest corrosion current and corrosion inhibition efficiency were found to be of 0.194 μA/cm² and 99.15%, respectively, for 60% mGO-ODA/MAPP. In summary, we

report a promising method to fabricate high-performance graphene-based composites, which can be successfully utilized as the gas barrier and anticorrosion coating materials.

Acknowledgments

Appendix A. Supplementary material

Supplementary data associated with this article can be found in the online version at http://dx.doi.org/10.1016/j.memsci.2017.10.031.

References

[1] P. Tzeng, B. Stevens, I. Devlaming, J.C. Grunlan, Polymer-graphene oxide quad layer thin-film assemblies with improved gas barrier, Langmuir 31 (2015) 5919–5927.

[2] P. Bandyopadhyay, W.B. Park, R.K. Layek, M.E. Uddin, N.H. Kim, H.G. Kim, J.H. Lee, Hexylamine functionalized reduced graphene oxide/polyurethane nanocomposite-coated nylon for enhanced hydrogen gas barrier film, J. Memb. Sci. 500 (2016) 106–114.

[3] P. Tzeng, E.L. Lugo, G.D. Mai, B.A. Wilhite, J.C. Grunlan, Super hydrogen and helium barrier with polyelectrolyte nanobrick wall thin film, Macromol. Rapid Comm. 36 (2015) 96–101.

[4] R. Rajasekar, N.H. Kim, D. Jung, T. Kuila, J.K. Lim, M.J. Park, J.H. Lee, Electrostatically assembled layer-by-layer composites containing graphene oxide for enhanced hydrogen gas barrier application, Compos. Sci. Technol. 89 (2013) 167–174.

[5] O. Yucel, E. Unsal, J. Harvey, M. Graham, D.H. Jones, M. Cakmak, Mechanisms of drying of graphene/poly (amide imide) solutions for films with enhanced gas barrier and mechanical as investigated by real time measurement system, J. Memb. Sci. 495 (2015) 65–71.

[6] O.C. Compton, S. Kim, C. Pierre, J.M. Torkelson, S.T. Nguyen, Crumpled graphene nanosheets as highly effective barrier property enhancers, Adv. Mater. 22 (2010) 4759–4763.

[7] H.D. Huang, P.G. Ren, J.Z. Xu, L. Xu, G.J. Zhong, B.S. Hsiao, Z.M. Li, Improved barrier properties of poly(lactic acid) with randomly dispersed graphene oxide nanosheets, J. Memb. Sci. 464 (2014) 110–118.

[8] Y.H. Yang, L. Bolling, M.A. Priolo, J.C. Grunlan, Super gas barrier and selectivity of graphene oxide-polymer multilayer thin films, Adv. Mater. 25 (2013) 503–508.

[9] I. Soltania, S.D. Smithb, R.J. Spontak, Effect of polyelectrolyte on the barrier efficacy of layer-by-layer nanoclay coatings, J. Memb. Sci. 526 (2017) 172–180.

[10] K. Kalaitzidou, H. Fukushima, L.T. Drzal, Multifunctional polypropylene composites produced by incorporation of exfoliated graphite nanoplatelets, Carbon 45 (2007) 1446–1452.

[11] J.A. Prince, S. Bhuvana, V. Anbharasi, N. Ayyanar, K.V.K. Boodhoo, G. Singh, Ultra-wetting graphene-based membrane, J. Memb. Sci. 500 (2016) 76–85.

[12] H. Kim, A.A. Abdala, C.W. Macosko, Graphene/polymer nanocomposites, Macromolecules 43 (2010) 6515–6530.

[13] W. Sun, L.D. Wang, T.T. Wu, M. Wang, Z.Q. Yang, Y.Q. Pan, G.C. Liu, Inhibiting the corrosion-promotion activity of graphene, Chem. Mater. 27 (2015) 2367–2373.

[14] Y.H. Yu, Y.Y. Lin, C.H. Lin, C.C. Chan, Y.C. Huang, High-performance polystyrene/graphene-based nanocomposites with excellent anti-corrosion properties, Polym. Chem. 5 (2014) 535–550.

[15] D. Prasai, J.C. Tuberquia, R.R. Harl, G.K. Jennings, K.I. Bolotin, Graphene: corrosion-inhibiting coating, ACS Nano 6 (2012) 1102–1108.

[16] D. Kang, J.Y. Kwon, H. Cho, J.H. Sim, H.S. Hwang, C.S. Kim, Y.J. Kim, R.S. Ruoff, H.S. Shin, Oxidation resistance of iron and copper foils coated with reduced graphene oxide multilayers, ACS Nano 6 (2012) 7763–7769.

[17] N.T. Kirkland, T. Schiller, N. Medhekar, N. Birbilis, Exploring graphene as a corrosion protection barrier, Corros. Sci. 56 (2012) 1–4.

[18] M. Schriver, W. Regan, W.J. Gannett, A.M. Zaniewski, M.F. Crommie, A. Zettl, Graphene as a long-term metal oxidation barrier: worse than nothing, ACS Nano 7 (2013) 5763–5768.

[19] K.C. Chang, W.F. Ji, M.C. Lai, Y.R. Hsiao, C.H. Hsu, T.L. Chuang, Y. Wei, J.M. Yeh, W.R. Liu, Synergistic effects of hydrophobicity and gas barrier properties on the anticorrosion property of PMMA nanocomposite coatings embedded with graphene nanosheets, Polym. Chem. 5 (2014) 1049–1056.

[20] C.H. Chang, T.C. Huang, C.W. Peng, T.C. Yeh, H.I. Lu, W.I. Hung, C.J. Weng, T.I. Yang, J.M. Yeh, Novel anticorrosion coatings prepared from polyaniline/graphene composites, Carbon 50 (2012) 5044–5051.

[21] X.X. Sheng, W.X. Cai, L. Zhong, D.L. Xie, X.Y. Zhang, Synthesis of functionalized graphene/polyaniline nanocomposites with effective synergistic reinforcement on anticorrosion, Ind. Eng. Chem. Res. 55 (2016) 8576–8585.

[22] M.T. Mo, W.J. Zhao, Z.F. Chen, Q.X. Yu, Z.D. Zeng, X.J. Wu, Q. Xue, Excellent tribological and anti-corrosion performance of polyurethane composite coatings reinforced with functionalized graphene and graphene oxide nanosheets, RSC Adv. 5 (2015) 56486–56497.

[23] M.E. Uddin, R.K. Layek, H.Y. Kim, N.H. Kim, D. Hui, J.H. Lee, Preparation and enhanced mechanical properties of non-covalently-functionalized graphene oxide/cellulose acetate nanocomposites, Compos. Part B-Eng. 90 (2016) 223–231.

[24] R.K. Layek, A.K. Nandi, A review on synthesis and properties of polymer functionalized graphene, Polymer 54 (2013) 5087–5103.

[25] S. Roy, X.Z. Tang, T. Das, L.Y. Zhang, Y.M. Li, S. Ting, X. Hu, C.Y. Yue, Enhanced molecular level dispersion and interface bonding at low loading of modified graphene oxide to fabricate super nylon 12 composites, ACS Appl. Mater. Interfaces 7 (2015) 3142–3151.

[26] W.J. Li, X.Z. Tang, H.B. Zhang, Z.G. Jiang, Z.Z. Yu, X.S. Du, Y.W. Mai, Simultaneous surface functionalization and reduction of graphene oxide with octadecylamine for electrically conductive polystyrene composites, Carbon 49 (2011) 4724–4730.

[27] F. You, D.R. Wang, X.X. Li, M.J. Liu, G.H. Hu, Z.M. Dang, Interfacial engineering of polypropylene/graphene nanocomposites: improvement of graphene dispersion by using tryptophan as a stabilizer, RSC Adv. 4 (2014) 8799–8807.

[28] S.H. Ryu, A.M. Shanmugharaj, Influence of long-chain alkylamine-modified graphene oxide on the crystallization, mechanical and electrical properties of isotactic polypropylene nanocomposites, Chem. Eng. J. 244 (2014) 552–560.

[29] M.F. Diop, J.M. Torkelson, Maleic anhydride functionalization of polypropylene with suppressed molecular weight reduction via solid-state shear pulverization, Polymer 54 (2013) 4143–4154.

[30] X.Q. Jia, M. Herrera-Alonso, T.J. McCarthy, Nylon surface modification. Part 1. targeting the amide groups for selective introduction of reactive functionalities, Polymer 47 (2006) 4916–4924.

[31] R.K. Layek, A.K. Das, M.U. Park, N.H. Kim, J.H. Lee, Layer-structured graphene oxide/polyvinyl alcohol nanocomposites: dramatic enhancement of hydrogen gas barrier properties, J. Mater. Chem. A 2 (2014) 12158–12161.

[32] H.Y. Liu, T. Kuila, N.H. Kim, B.C. Ku, J.H. Lee, In situ synthesis of the reduced graphene oxide-polyethyleneimine composite and its gas barrier properties, J. Mater. Chem. A 1 (2013) 3739–3746.

[33] N.I. Kovtyukhova, P.J. Ollivier, B.R. Martin, T.E. Mallouk, S.A. Chizhik, E.V. Buzaneva, A.D. Gorchinskiy, Layer-by-layer assembly of ultrathin composite films from micron-sized graphite oxide sheets and polycations, Chem. Mater. 11 (1999) 771–778.

[34] W.S. Hummers, R.E. Offeman, Preparation of graphitic oxide, J. Am. Chem. Soc. 80 (1958) (1339–1339).

[35] J.M.S. Henis, M.K. Tripodi, Composite hollow fiber membranes for gas separation - the resistance model approach, J. Memb. Sci. 8 (1981) 233–246.

[36] I. Pinnau, J.G. Wijmans, I. Blume, T. Kuroda, K.V. Peinemann, Gas permeation through composite membranes, J. Memb. Sci. 37 (1988) 81–88.

[37] X.Y. Tang, T. Mei, J. Yang, C.A. Zhang, M.J. Lv, X.B. Wang, Synthesis and characterization of alkylamine-functionalized graphene for polyolefin-based nanocomposites, Appl. Surf. Sci. 305 (2014) 725–731.

[38] S. Stankovich, D.A. Dikin, R.D. Piner, K.A. Kohlhaas, A. Kleinhammes, Y. Jia, Y. Wu, S.T. Nguyen, R.S. Ruoff, Synthesis of graphene-based nanosheets via chemical reduction of exfoliated graphite oxide, Carbon 45 (2007) 1558–1565.

[39] W.F. Chen, L.F. Yan, P.R. Bangal, Chemical reduction of graphene oxide to graphene by sulfur-containing compounds, J. Phys. Chem. C 114 (2010) 19885–19890.

[40] P. Bandyopadhyay, T.T. Nguyen, X.Y. Li, N.H. Kim, J.H. Lee, Enhanced hydrogen gas barrier performance of diaminoalkane functionalized stitched graphene oxide/polyurethane composites, Compos. Part B-Eng. 117 (2017) 101–110.

[41] S.P. Zhang, H.O. Song, Supramolecular graphene oxide-alkylamine hybrid materials: variation of dispersibility and improvement of thermal stability, New J. Chem. 36 (2012) 1733–1738.

[42] W.H. Liao, S.Y. Yang, J.Y. Wang, H.W. Tien, S.T. Hsiao, Y.S. Wang, S.M. Li, C.C.M. Ma, Y.F. Wu, Effect of molecular chain length on the mechanical and thermal properties of amine-functionalized graphene oxide/polyimide composite films prepared by in situ polymerization, ACS Appl. Mater. Interfaces 5 (2013) 869–877.

[43] S.M. Zhao, F.H. Chen, C.Z. Zhao, Y.J. Huang, J.Y. Dong, C.C. Han, Interpenetrating network formation in isotactic polypropylene/graphene composites, Polymer 54 (2013) 3680–3690.

[44] X. Wang, Y.A. Hu, L. Song, H.Y. Yang, W.Y. Xing, H.D. Lu, In situ polymerization of graphene nanosheets and polyurethane with enhanced mechanical and thermal properties, J. Mater. Chem. 21 (2011) 4222–4227.

[45] T. Kuila, S. Bose, A.K. Mishra, P. Khanra, N.H. Kim, J.H. Lee, Effect of functionalized graphene on the physical properties of linear low density polyethylene nanocomposites, Polym. Test. 31 (2012) 31–38.

[46] Z. Xu, C. Gao, In situ polymerization approach to graphene-reinforced nylon-6 composites, Macromolecules 43 (2010) 6716–6723.

[47] W.B. Park, P. Bandyopadhyay, T.T. Nguyen, T. Kuila, N.H. Kim, J.H. Lee, Effect of high molecular weight polyethyleneimine functionalized graphene oxide coated polyethylene terephthalate film on the hydrogen gas barrier properties, Compos. Part B-Eng. 106 (2016) 316–323.

[48] L.L. Zhao, H.Y. Zhang, N.H. Kim, D. Hui, J.H. Lee, Q. Li, H.X. Sun, P. Li, Preparation of graphene oxide/polyethyleneimine layer-by-layer assembled film for enhanced hydrogen barrier property, Compos. Part B-Eng. 92 (2016) 252–258.

[49] C.Y. Cho, F. Xiang, K.L. Wallace, J.C. Grunlan, Combined ionic and hydrogen bonding in polymer multi layer thin film for high gas barrier and stretchiness, Macromolecules 48 (2015) 5723–5729.

[50] K.H. Lee, J. Hong, S.J. Kwak, M. Park, J.G. Son, Spin self-assembly of highly ordered multilayers of graphene-oxide sheets for improving oxygen barrier performance of

polyolefin films, Carbon 83 (2015) 40–47.

[51] T.C. Huang, T.C. Yeh, H.Y. Huang, W.F. Ji, Y.C. Chou, W.I. Hung, J.M. Yeh, M.H. Tsai, Electrochemical studies on aniline-pentamer-based electroactive polyimide coating: corrosion protection and electrochromic properties, Electrochim. Acta 56 (2011) 10151–10158.

[52] R.X. Yuan, S.Q. Wu, P. Yu, B.H. Wang, L.W. Mu, X.G. Zhang, Y.X. Zhu, B. Wang, H.Y. Wang, J.H. Zhu, Superamphiphobic and electroactive nanocomposite toward self cleaning, antiwear, and anticorrosion coatings, ACS Appl. Mater. Interfaces 8 (2016) 12481–12493.

[53] N. Sarkar, G. Sahoo, R. Das, G. Prusty, D. Sahu, S.K. Swain, Anticorrosion performance of three-dimensional hierarchical PANI@BN nanohybrids, Ind. Eng. Chem. Res. 55 (2016) 2921–2931.

[54] K.C. Chang, M.H. Hsu, H.I. Lu, M.C. Lai, P.J. Liu, C.H. Hsu, W.F. Ji, T.L. Chuang, Y. Wei, J.M. Yeh, W.R. Liu, Room-temperature cured hydrophobic epoxy/graphene composites as corrosion inhibitor for cold-rolled steel, Carbon 66 (2014) 144–153.

[55] E. Husain, T.N. Narayanan, J.J. Taha-Tijerina, S. Vinod, R. Vajtai, P.M. Ajayan, Marine corrosion protective coatings of hexagonal boron nitride thin films on stainless steel, ACS Appl. Mater. Interfaces 5 (2013) 4129–4135.